

Approaching Artery Rigid Dynamics in IVUS

Aura Hernández-Sabaté*, Debora Gil, Eduard Fernandez-Nofrerias, Petia Radeva, and Enric Martí

Abstract—Tissue biomechanical properties (like strain and stress) are playing an increasing role in diagnosis and long-term treatment of intravascular coronary diseases. Their assessment strongly relies on estimation of vessel wall deformation. Since intravascular ultrasound (IVUS) sequences allow visualizing vessel morphology and reflect its dynamics, this technique represents a useful tool for evaluation of tissue mechanical properties. Image misalignment introduced by vessel–catheter motion is a major artifact for a proper tracking of tissue deformation. In this work, we focus on compensating and assessing IVUS rigid in-plane motion due to heart beating. Motion parameters are computed by considering both the vessel geometry and its appearance in the image. Continuum mechanics laws serve to introduce a novel score measuring motion reduction in *in vivo* sequences. Synthetic experiments validate the proposed score as measure of motion parameters accuracy; whereas results in *in vivo* pullbacks show the reliability of the presented methodologies in clinical cases.

Index Terms—Fourier analysis, intravascular ultrasound (IVUS) dynamics, longitudinal motion, quality measures, tissue deformation.

I. INTRODUCTION

CLINICAL effectiveness of intravascular treatments (such as stent placement [1] or atherosclerotic disease assessment [2]) depend, among other factors, on tissue biomechanical properties. Arterial tissue elastic properties and detection of rupture-prone vulnerable plaques, in particular, are one of the most active areas of research in both the cardiology and biomedical imaging communities [1]–[4]. The main mechanical properties currently under study are radial strain, which is related to plaque type and vulnerability [4], and shear stress, which influences the probability of plaque accumulation [1]. Both measures can be computed by means of the study of vessel tissue deformation along the cardiac cycle.

Conventional 2-D intravascular ultrasound (IVUS) is a powerful imaging tool that enables the assessment of different kind of vessel plaques and the visualization of arterial 3-D models.

Manuscript received December 29, 2008; revised March 03, 2009. First published April 14, 2009; current version published October 28, 2009. This work was supported in part by the Spanish projects PI071188 and CONSOLIDER-INGENIO 2010 (CSD2007-00018). The work of D. Gil was supported by The Ramon y Cajal Program. *Asterisk indicates corresponding author.*

*A. Hernández is with the Computer Science Department, Universitat Autònoma de Barcelona, 08193 Bellaterra, Spain and also with the Computer Vision Center, 08193 Bellaterra, Spain (e-mail: aura@cvc.uab.cat).

D. Gil and E. Martí are with the Computer Science Department of Universitat Autònoma de Barcelona, 08193 Bellaterra, Spain, and the Computer Vision Center, 08193 Bellaterra, Spain.

E. Fernandez is with the Hospital Universitari Germans Trias i Pujol, 08916 Badalona, Spain.

P. Radeva is with the Applied Mathematics Dept. of Univ. de Barcelona, Barcelona, Spain, and the Computer Vision Center, 08193 Bellaterra, Spain.

Digital Object Identifier 10.1109/TMI.2009.2017927

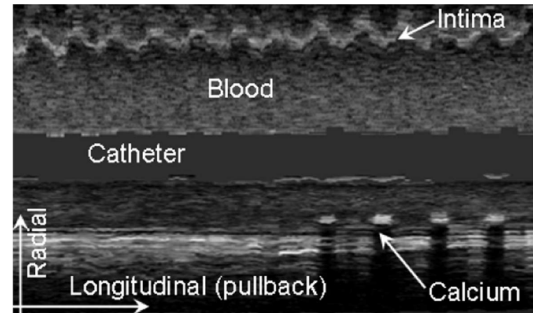


Fig. 1. Artifacts in longitudinal cut appearance induced by cardiac motion.

Cardiac dynamics introduces a misalignment of vessel structures in short axis views as well as a saw-tooth-shape of the vessel appearance in longitudinal views that hinders accuracy of volumetric measures and evaluation of tissue deformation [5]. The longitudinal cut shown in Fig. 1 illustrates the two main artifacts induced by vessel dynamics in *in vivo* pullbacks. The upper profile shows the saw-tooth-shape pattern of the vessel intima wall (dark line) introduced by relative vessel–catheter translation. The bottom profile presents a structure misalignment due to the relative vessel–catheter rotation for an echo-shadowing calcified plaque.

A usual way to minimize the impact of dynamics is the use of ECG-gated devices [6] and image-based gating methods [7]. Both of them return a static sequence by either capturing frames synchronized with heart dynamics [6] or discarding those frames not synchronized with it [7]. In any case, without a 4-D model of the artery [8], only a static model of the artery at end diastole is reliable. Such models are suitable for volumetric measurements, visualization, and palpography techniques measuring peak tissue deformation. However, for a continuous assessment of tissue elastic properties, one should consider all frames between systole and diastole [9], [10]. Due to artery longitudinal dynamics, this has only been achieved, so far, by 4-D fusion of angiography and IVUS pullbacks [8].

The complex motion of the imaging catheter inside the coronary vessels causes two main motion artifacts in IVUS sequences: 1) in-plane rigid motion (vessel–catheter translation and rotation) and 2) forward and backward longitudinal motion along the catheter axis [11]. Longitudinal motion disturbs computation of tissue properties only in the case that the pullback goes through a segment presenting a transition between two different kind of plaque. Even if we account for longitudinal motion, transitional segments might not yield a reliable estimation of tissue elastic properties and, thus, deserve special treatment. In this paper we explore in-plane rigid dynamics for improvement of vessel physical properties evaluation [9], [10], [12].

Current approaches for motion compensation in IVUS work on three main domains: image intensity [10], [12], radio-frequency (RF) signal [13], and vessel geometric appearance [9]. Intensity-based approaches rely on either registration [10] or tracking [12] strategies. In the case of large displacements, tracking [12] fails to yield the expected results, whereas registration [14] requires exhaustive (computationally inefficient) search of the parametric space. Moreover, changes in image intensity from one frame to the next one substantially affect the performance of intensity-based algorithms. Explicit formulae of motion parameters overcome the limitation of capture range, whereas the impact of morphological changes is reduced by including geometric considerations to the algorithm. In this fashion, the motion artifact reduction developed in [9] achieves good results, as long as, only catheter translation compensation is required. An alternate way of dealing with image intensity changes is considering the RF signal [13]. On one hand, although IVUS images are reconstructed from RF signals, not all IVUS devices allow recording and exporting such signals. On the other hand, vessel translation is given by the difference between the position of the center of the catheter and the center of the vessel. Since the RF domain is defined in polar coordinates centered at the catheter, translations are not straightforward and, in fact, existing algorithms based on RF signals only address rotations.

We propose modelling image in-plane dynamics as a rigid body motion [15], which is given in terms of a translation followed by a rotation. We provide explicit formulae for motion parameters by combining vessel appearance and shape. In order to allow a complete exploring of vessel dynamics, we decompose motion into a geometric term due to vessel shape and a dynamic one induced by heart beating and breathing. We take special care in defining an objective score to assess parameters accuracy in real data and introduce a novel quality score measuring image alignment. Two sets of experiments are presented: validation on synthetic sequences and performance in real pull-backs. Synthetic experiments assess the accuracy of motion parameters and validate our quality score. Results on *in vivo* pull-backs show the score correlation to visual appearance of longitudinal cuts. Finally, we present a first approximation to image based ECG gating.

The remainder of the paper is structured as follows. In Section II we describe our dynamical model and in Section III we decouple motion geometric and dynamic terms. The quality measure is defined in Section IV. Experiments on synthetic and real sequences are exposed in Sections V and VI. Finally, discussions and conclusions are explained in Section VII.

II. CROSS SECTION DYNAMICS

A. Rigid Body Motion

The dynamics of coronary arteries is mainly governed by the left ventricle motion, blood pressure, and artery geometric properties [16]–[18]. The first order-approximation to vessel dynamics is given by a linear transformation combining translation, rotation, and scaling [19]. Given that size changes are important indicators for artery properties (distensibility and compliance), scaling compensation is not addressed. Rigid motion

is given by a rotation followed by a translation and can be modelled as a rigid body motion.

Rigid body dynamics is determined by means of the center of gravity or mass since it is the point describing the object response to external forces and torques [20]. In this framework, the object motion is given by a rotation centered at its center of mass, which position is identified to the object translation. If the center of mass of the object at time zero is taken as origin, then the linear application mapping the object at a given time to the object at time zero is given by

$$\begin{pmatrix} \tilde{x} \\ \tilde{y} \end{pmatrix} = \begin{pmatrix} \cos(\theta) & -\sin(\theta) \\ \sin(\theta) & \cos(\theta) \end{pmatrix} \begin{pmatrix} x - t_x \\ y - t_y \end{pmatrix} \quad (1)$$

for $t = (t_x, t_y)$ the position of the center of mass and θ the angle of rotation in radians. In the case of IVUS sequences, rigid motion parameters are computed by combining vessel geometry and appearance as follows.

B. Vessel Translation

The translation aligning a given frame to a reference frame is determined by the center of mass of the vessel (namely VCM) at such frame. In IVUS sequences, images are reconstructed from the reflection of an ultrasound beam against particles and, thus, grey level reflects tissue mass density [21], [22]. Therefore, the center of mass given by the image intensity (namely ICM) corresponds to the physical center of gravity of the vessel. However, some acquisition devices allow interactive tuning of the image brightness in order to enhance tissue and vessel structures appearance [23]. Since such intensity gain is radial [24], tissue close to the catheter might look brighter. Thus, for vessels not centered at the catheter, intensity gainings might deviate the position of ICM from the true center of mass. Although the vessel geometric center (namely GCM) only coincides with the center of mass in the case of uniform tissue density, we use it to compensate the deviation of ICM for noncentered vessels.

The image center mass ICM is given by averaging image pixel positions, (i, j) , weighted by their grey-value intensity

$$\text{ICM} = \left(\frac{\sum_{i=1}^n i \sum_{j=1}^m I(i, j)}{\sum_{i=1}^n \sum_{j=1}^m I(i, j)}, \frac{\sum_{j=1}^m j \sum_{i=1}^n I(i, j)}{\sum_{i=1}^n \sum_{j=1}^m I(i, j)} \right)$$

for n and m the number of rows and columns of the image.

The geometric center, GCM, of a set of N image points, $(x_k, y_k)_{k=1}^N$, is computed as the average of their positions

$$\text{GCM} = \frac{1}{N} \left(\sum_{k=1}^N x_k, \sum_{k=1}^N y_k \right).$$

In our case, the points are a set roughly lying on the transition between media and adventitia layers, since it is the vessel structure best preserving its shape regardless of morphological changes. The detection of adventitia points [25] is two-fold. First, vessel translation induced by heart motion is reduced by taking as origin the image center of mass ICM. Then, points roughly lying on the adventitia can be extracted by means of negative horizontal edges of the polar image centered at ICM as detailed in [25]. The set $(x_k, y_k)_k$ is obtained by transforming their polar (radial and angular) coordinates to the Cartesian domain.

The geometric center of mass is used to correct the center ICM in the measure that the vessel wall is not centered at the catheter. Consider the maximum, R_{\max} , and minimum, R_{\min} , distances of the set $(x_k, y_k)_k$ to the image center

$$R_{\max} = \max_k \left(\sqrt{x_k^2 + y_k^2} \right) \quad R_{\min} = \min_k \left(\sqrt{x_k^2 + y_k^2} \right).$$

And let DR note the vessel–catheter deviation rate given by

$$\text{DR} = \frac{R_{\min}}{R_{\max}}.$$

Then, the vessel center of mass, VCM, is defined as

$$\text{VCM} = \text{DR} \cdot \text{ICM} + (1 - \text{DR}) \cdot \text{GCM}. \quad (2)$$

C. Vessel Rotation Angle

Once vessel translation has been compensated, two global motions still remain: rotation and radial scaling. Although this paper does not address radial scaling, in the polar domain with origin VCM, they convert into a horizontal translation (corresponding to rotation) and a vertical scaling, (corresponding to radial scaling)

$$I_2(i, j) = I_1(i + t, \lambda j)$$

for I_1, I_2 two consecutive polar frames (with origin at VCM) of the sequence. In the case of human coronary arteries, scaling is very close to 1 [26], so $\lambda = 1 + \varepsilon$ becomes a perturbation of identity given by ε . Furthermore, we restrict computations to a band around the media-adventitia layer, given by $j = j_0 + \Delta j$. By Taylor's formula, it follows that the first-order approximation to I_2 is given by

$$\begin{aligned} I_2(i, j) &= I_1(i + t, j + \varepsilon j) \sim I_1(i + t, j) \\ &\quad + \varepsilon j \partial_j I_1(i + t, j) \\ &= I_1(i + t, \Delta j + j_0) \\ &\quad + \varepsilon j \partial_j I_1(i + t, j) \sim I_1(i + t, \Delta j + j_0) \end{aligned}$$

for ∂_j denoting the partial derivative with respect to the second variable.

Since t and j_0 are constant shifts, the first-order approximation to I_2 can be computed by applying the Fourier transform [27] and using phase correlation [28]. Let \hat{I}_1, \hat{I}_2 be the Fourier transforms of I_1, I_2 and let us assume that they differ in a pure translation

$$I_2(i, j) = I_1(i - t_1, j - t_2) [= I_1(i + t, \Delta j + j_0)]$$

then their Fourier transforms are related via

$$\hat{I}_2(\omega) = \hat{I}_1(\omega) e^{-i\langle \omega, t \rangle}$$

for $\omega = (\omega_1, \omega_2)$ the Fourier frequency and $\langle \omega, t \rangle = \omega_1 t_1 + \omega_2 t_2$ the Euclidean scalar product.

If we consider the phase, $\rho(\omega)$, of the ratio between the two Fourier transforms [29], we have that

$$\begin{aligned} \rho(\omega) &= \rho \left(\frac{\hat{I}_2(\omega)}{\hat{I}_1(\omega)} \right) \\ &= \rho \left(e^{-i\langle \omega, t \rangle} \right) = \langle \omega, t \rangle = \omega_1 t_1 + \omega_2 t_2 \end{aligned}$$

so that the points $(\omega_1, \omega_2, \rho(\omega))$ lie on a plane, Π , with the slopes given by the translation

$$\Pi : \rho(\omega) = t_1 \omega_1 + t_2 \omega_2.$$

In practice, noise and texture introduce a scatter in the set $(\omega_1, \omega_2, \rho(\omega))$, especially for those frequencies with smaller amplitudes. We reduce noise-scatter by only considering those frequencies common to both images with an associated amplitude larger than a given percentile. Such frequencies with the phase ρ yield a point cloud, which regression plane provides a least-square estimator of the plane Π .

The first slope of the regression plane is our estimation of the angle of rotation between two consecutive frames. Rotation angles are given in the range $[-180^\circ, 180^\circ]$, which cover all possible rotational motions. The rotation of each image at time k with respect to a reference frame at time 1 is computed by accumulating all frame-to-frame rotation angles. Let $\theta^{k-1, k}$ be the rotation angle between two consecutive frames at times $k-1$ and k , then the rotation angle aligning the k th frame to a first one is given by

$$\theta^k := \sum_{j=1}^{j=k} \theta^{k-1, k}. \quad (3)$$

The reliability of the rotation angle is related to the regression plane fitting error (residuals). Large residuals indicate a poor linear dependency between frequency and phase. In this cases, the estimated parameter does not properly approach the rotation angle and should be discarded. Since our polar images are 360 pixels wide, anomalous cases are detected by a mean fitting error over 1 (degree/pixel). Such angles constitute less than 6.43% of the data analyzed and their values are interpolated along the sequence using the preserved angles.

D. IVUS Dynamics Compensation

We align sequence frames to a first reference frame by applying (1) to the k th image

$$\begin{pmatrix} \tilde{x} \\ \tilde{y} \end{pmatrix} = \begin{pmatrix} \cos(\theta^k) & -\sin(\theta^k) \\ \sin(\theta^k) & \cos(\theta^k) \end{pmatrix} \begin{pmatrix} x - \text{VCM}_x^k \\ y - \text{VCM}_y^k \end{pmatrix}$$

for θ^k given by formula (3) and $\text{VCM}^k = (\text{VCM}_x^k, \text{VCM}_y^k)$ given by applying (2) to frame k . Images are corrected by transforming to polar coordinates with origin VCM^k ; horizontally shifting polar images θ^k degrees and converting to the cartesian domain with origin, $(0, 0)$, at the image center.

III. DYNAMICS EXPLORING

The rigid motion that cardiac vessels undergo is a complex dynamical process which results from the combination of several contributions. In general, it presents a geometric component related to the artery 3-D shape and a dynamic one induced by breathing and cardiac movements [22]. Depending on the particular problem we approach, each of the terms should have specific treatment. Exploring artery geometry might be derived by analyzing the geometric component [30], whereas extraction of cardiac dynamics concerns the cardiac dynamical contribution [31]. In the case of vessel biomechanics analysis, the goal is to produce a static model allowing a better tissue tracking along the segment. Firstly, we note that, without further analysis, the geometric component does not reach a reliable 3-D representation of the vessel geometry, which might lead to wrong static models. Secondly, even if we could infer the true 3-D geometry from it, by compensating vessel tortuosity we have no guarantee of a better alignment of vessel plaque. Therefore we suggest correcting only the dynamical terms of the translation and rotation for stabilizing the sequence.

In order to allow a complete comprehension of vessel dynamics, in this section we provide the mathematical tools for decoupling each of the terms. The subindex g will denote the geometric term of a motion parameter, the subindex c the one induced by heart beating and the subindex b breathing contributions. As usual, Fourier transforms will be indicated by a hat ($\hat{\cdot}$) over functions. The translation and rotation parameters are functions of the time s . Using these notations, we have that the angle and translation decompose into

$$\begin{aligned} t(s) &= t_g(s) + t_b(s) + t_c(s) \\ \theta(s) &= \theta_g(s) + \theta_b(s) + \theta_c(s). \end{aligned} \quad (4)$$

Breathing and cardiac terms are periodic and, thus, have a discrete Fourier spectrum (Fourier series given by the principal harmonic), while geometry has a broadband (nondiscrete) spectrum [27]. Principal harmonics have been learned by supervised classification of the spectrum of a training set of 30 patients without apparent lesions used in a study for assessment of myocardial perfusion in contrast angiography [32]. Confidence intervals of the 95% yield the expected ranges for the principal frequency of each of the periodic components. For breathing it is (10,45) repetitions per minute (rpm), while for cardiac motion it is (45, 200) rpm.

We approach each term in (4) as follows. We model the artery geometric component [30] as a C^∞ function. Since the artery length is finite, the geometric component is a function of compact support and, thus, the derivatives of the geometric component are integrable functions. Therefore, its Fourier transform is of rapid decay, so that, high frequencies are negligible [33]. We approximate the geometric term by the frequencies between 1 and 10 rpm. The study reported in [32] indicates that, in spite of being periodic, breathing can be defined by the whole spectrum in the interval (10,45) rpm. Finally, cardiac motion principal harmonic, ω_c , is defined as the first local maximum in (45, 200) rpm and the term is approximated by the first 10 harmonics, $(k\omega_c)_{k=1:10}$.

It follows that the motion terms of a sequence lasting N_{Sec} seconds are given by

$$\begin{aligned} t_g(s) &= \frac{1}{T} \int_{I_g} \hat{t}(\omega) e^{i\omega s} d\omega \\ \theta_g(s) &= \frac{1}{T} \int_{I_g} \hat{\theta}(\omega) e^{i\omega s} d\omega \\ t_b(s) &= \frac{1}{T} \int_{I_b} \hat{t}(\omega) e^{i\omega s} d\omega \\ \theta_b(s) &= \frac{1}{T} \int_{I_b} \hat{\theta}(\omega) e^{i\omega s} d\omega \\ t_c(s) &= \frac{1}{T} \sum_{k=1}^{k=10} \hat{t}(k\omega_c) e^{ik\omega_c s} \\ \theta_c(s) &= \frac{1}{T} \sum_{k=1}^{k=10} \hat{\theta}(k\omega_c) e^{ik\omega_c s} \end{aligned} \quad (5)$$

where the period $T = N_{\text{Sec}}/60$ is the sequence length (in minutes) and defines the domains of integration as $I_g = (-10T, 10T)$ and $I_b = (-45T, -10T) \cup (10T, 45T)$.

Since, even in healthy cases, the heart rate varies along the pullback, the peaks in the Fourier series are spread around the theoretic harmonic frequencies. The more irregularities in periodicity we have, the more spread around the theoretic harmonic the Fourier development is. The harmonics less corrupted by noise are obtained by optical filtering [34]. The technique, widely used in electron crystallography, selects Fourier peaks by thresholding the difference between the amplitude achieved at the harmonic and an average of neighboring amplitudes. Harmonics selected by optical filtering are the only contributions to the sums in (5).

Fig. 2 shows the Fourier terms decoupling for the rotation angle in the top left plot. Vertical lines in the Fourier spectrum of the signal (bottom left plot) indicate the ranges defined for the three phenomena. Dots mark the 10 cardiac harmonics and squares the ones selected after optical filtering. The three components of the angle are shown in right plots.

IV. DYNAMICS QUALITY MEASURE

In real pullbacks there is no objective error measure indicating the amount of motion suppressed, since motion parameters are unknown. In most cases, quality measures are either subjective measures, based on the visual appearance of sequences and longitudinal cuts [7], or rely on extraction of vessel properties (such as strain in [10]). In this section, we develop an objective measure which is related to the accuracy of the estimated parameters.

In order to obtain an objective measure of the amount of motion suppressed two main issues should be addressed. Firstly, a similarity measure quantifying image changes along the sequence should be defined. The evaluation of the similarity measure on sequences before and after motion compensation provides two motion scores. A second stage concerns defining a criterion for comparing such scores.

Usual similarity measures (such as normalized mutual information [35] or normalized cross-correlation [36]) yield scalar values based on image intensity (overall) differences. Since they

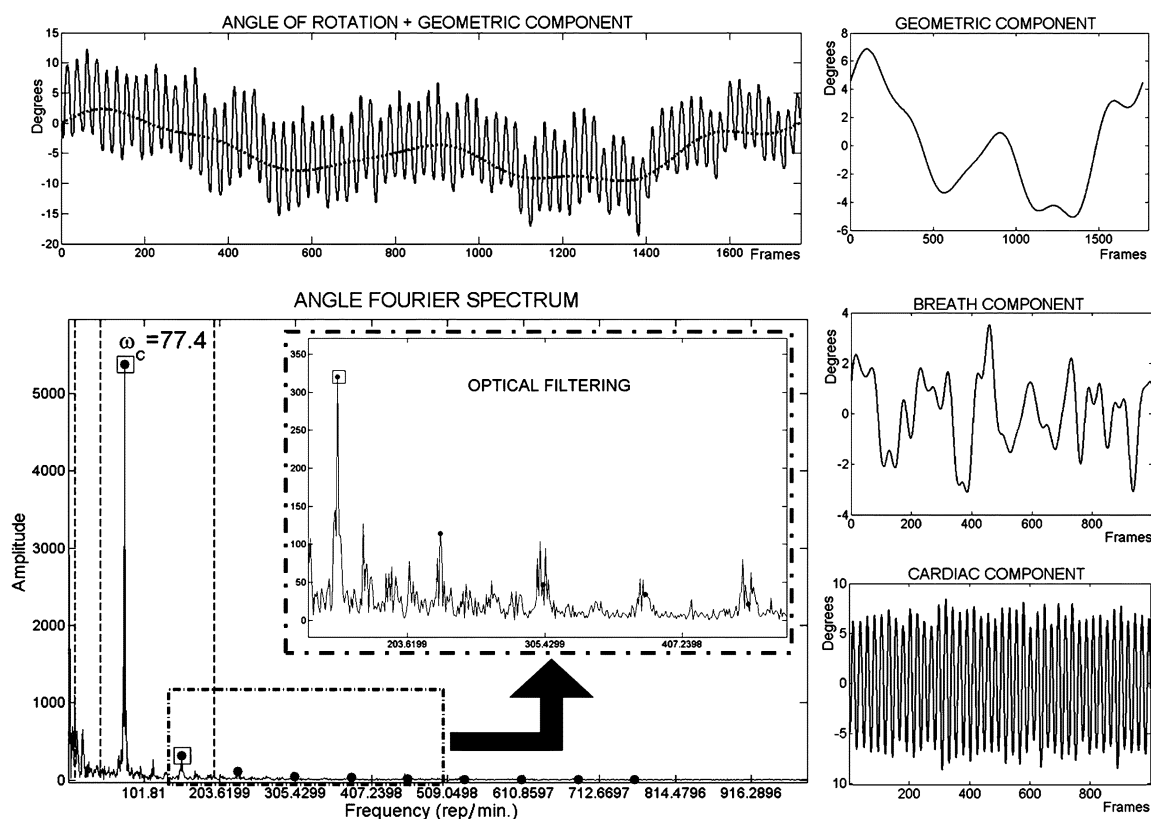


Fig. 2. Motion decomposition. Rotation angle and its Fourier decomposition on the left; geometric, breathing, and cardiac terms on the right.

reach an extreme value for aligned images, they are successfully applied to motion detection [10], [37]. In the case of assessing motion compensation in IVUS sequences, they present two main limitations:

- **Computation is sensitive to image digital quality.** In the case of intensity-based metrics (cross-correlation, sum of square differences, ...) texture and speckle might decrease their accuracy and force a previous image filtering [37]. In the case of probabilistic approaches (e.g., normalized mutual information) values are substantially affected by the number and distribution of histogram bins, which depend on grey-values range and resolution.
- **They provide a global estimation of the alignment rate.** Usual similarity measures are scalar scores computed, at most, over a region of interest. However, vessel motion is not visually noticed at all image pixels but only at some salient areas, such as calcium transitions or adventitia points of extreme curvature. This motivates adopting a local approach and tracking image motion for each pixel. Although cross-correlation and sum-of-square-differences support reliable computation in small neighborhoods (compared to information measures, which need a minimum number of samples for a reliable computation [35]), they are highly affected by image backscatter [37]. Thus, for small sets of pixels, their values might be (random) quantities due to noise.

Regarding the comparison criterion for motion scores computed before and after compensation, the following should be noted.

- **Extreme values are influenced by the anatomic and morphological differences along the vessel segment.** After motion correction, vessel displacement has disappeared, but morphological changes still remain. That is, even in the best case, comparison of aligned images along the sequence is prone to be a non-constant function depending on the particular morpho-geometric changes of the vessel segment. We claim that, in order to properly quantify vessel alignment, only the dynamic components should be taken into account.

By the above considerations, both, the similarity measure and the comparison criterion, should discard image areas where motion is not observed. Otherwise the score is prone to detect a random motion (due to dark areas, blood, and other artifacts) rather than the true vessel motion. This leads to considering a local approach for the definition of both quantities and only use values computed for those pixels which contribute relevant information about global alignment.

Inspired on strategies of classic fluid mechanics [38], we propose exploring the conservation of a physical quantity along the sequence. In particular, we use the local density of mass as it might be approximated by the image local mean, LM. We compute LM in sliding windows of size (empirically set) 9×9 pixels. The LM values for all images provide a pixel-wise function describing the conservation of the local density of mass along the sequence.

Concerning comparison before and after motion compensation, we propose comparing only cardiac terms [15]. Let \widehat{LM}_0 and \widehat{LM}_1 be the Fourier transforms of LM (or any other simi-

larity score) before (LM_0) and after (LM_1) correction and consider the cardiac frequency ω_c as given in Section III. We define the Cardiac Alignment Rate (CAR) as

$$CAR := 1 - \frac{A_{\widehat{LM}_1}(\omega_c)}{A_{\widehat{LM}_0}(\omega_c)} \quad (6)$$

for $A_{\widehat{LM}_0}(\omega_c)$ and $A_{\widehat{LM}_1}(\omega_c)$ the amplitudes corresponding to the cardiac frequency of \widehat{LM}_0 and \widehat{LM}_1 , respectively. The CAR index is close to 1 in the case that cardiac motion has been suppressed, whereas approaches zero (or becomes even negative) for a poor rate of motion reduction.

The CAR score is well suited for evaluating cardiac motion suppression at specific image areas (those showing motion in our case). In order to measure the reduction of (global) motion a score involving all valid CAR values should be defined.

Fig. 3 sketches the main steps involved in the computation of our quality measure: computation of the image descriptor (top block), conservation of local density along the sequence (middle block) and the CAR value for all pixels (bottom block). The first block illustrates the modelling of the local density of mass in terms of the image local mean. The local mean of the image (shown on the right hand side) is obtained by computing, for each pixel, the image mean on a window (white square on the left image) centered on each pixel (black point). In the second block, we have the evolution of the local mean at a single pixel before (left) and after (right) image alignment. The plot obtained before alignment presents a well defined periodic behavior; afterwards, although the periodic pattern has been suppressed, the function still presents a variability due to noise and morphologic changes. The third block shows the (sorted) CAR values obtained for all image pixels on the top plot, as well as, the position on the images of those pixels achieving extreme values (dotted squares on the CAR plot) at the bottom. Since we deal with a global movement, all pixels in an image should present a similar CAR value. However, at blood, uniform, and outer areas CAR achieves extreme low values (left bottom image), while pixels showing motion (like calcium–tissue transition on the right image) present a uniform (high) CAR value.

We define our conservation of density rate (CDR) as the trimmed mean [39] of the CAR value

$$CDR := \mu(\{CAR \mid CAR > \text{prct}\}) * 100$$

for prct a given percentile. We have experimentally checked that CDR computed for the superior 66% percentile statistically compares (in the sense of random variables) to the angle relative accuracy (Section V-A and [40]).

V. VALIDATION PROTOCOL

A. Synthetic Data

Our synthetic experiments focus on addressing the following.

- **Accuracy of the motion parameters estimation.** Rigid motion requires computing two parameters: translation and rotation. Translation accuracy depends on the vessel center of mass, while rotation angle relies on the ability of Fourier analysis for computing global translation. The center of mass bases on the estimation of vessel walls geometry and,

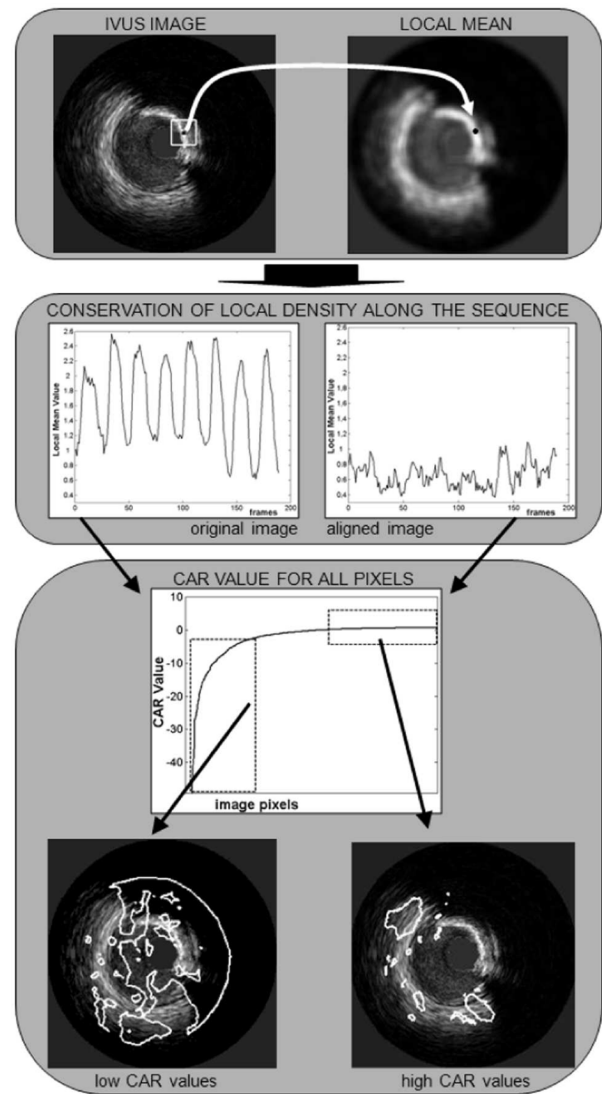


Fig. 3. Quality measure computation.

thus, its accuracy depends on the appearance of vessel morphology. Concerning angle estimation, the first component of the translation given by Fourier analysis on polar images estimates the rotation angle as far as the center of mass is accurate. Any deviation makes the horizontal component underestimate the rotation angle, since it would also decompose into a vertical shift. We have generated computational dynamic phantoms simulating different vessel morphologies and motion patterns.

- **Reliability of CDR as measure of parameters accuracy.** The motion parameters used for generating the phantoms constitute the ground truth. The absolute and relative errors for the difference between estimated and ground truth parameters are our quality measures. In order to validate CDR we have compared it to the relative accuracy of the rotation angle (see Section V-C). We have chosen the angle relative accuracy since its computation depends on the center of mass and, thus, it reflects the overall error. We also report results obtained for the cross-correlation (CC) computed on LM images.

Our computational phantoms have been created by applying a rigid motion [given by (1)] to still sequences distilled from real pullbacks. We have considered two motion models.

- 1) **Synthetic Profiles.** In order to illustrate that there are no limits in parameters range, synthetic motions simulate a frame-to-frame angular step of 1° and 10° . Two different patterns have been considered: a periodic sinusoidal motion (with several amplitudes and frequencies in the cardiac range) and a quadratic function.
- 2) **In vivo Profiles.** In order to produce motions as realistic as possible we have used motion parameters extracted from *in vivo* sequences using our methodology. Since performance relies on the translation accuracy (strongly dependant on vessel appearance), errors do not benefit from using motion patterns computed with our methodology. We have considered five *in vivo* motion patterns.

Regarding vessel morphologies, we have used two models.

- 1) **Static Model.** It is based on a unique image repeated 200 times simulating a sequence block of a motionless artery pullback. Errors for this model constitute the lower bound for the methodology accuracy.
- 2) **Sequence-based Model.** It is obtained by compensating motion of *in vivo* pullbacks and detects the sensitivity to varying morphologies (see Fig. 4). We have taken five vessel segments not belonging to the set used for extracting motion patterns.

B. In Vivo Data

Performance in real pullbacks has been validated in 32 vessel segments from clinical cases of the Hospital Universitari “Germans Trias i Pujol” in Badalona, Spain:

- 17 Left Anterior Descending (3 ostial, 2 proximal, and 12 medium);
- 11 Right Coronary (2 ostial, 5 proximal, and 4 medium);
- 4 Left main Coronary (2 medium and 2 distal).

Sequences have been recorded using a Galaxy–BostonSci device at 40 MHz with a rotating single transducer and constant pullback (0.5 mm/s). The digitalization rate was 30 fps and digitized images were 480×480 pixels with a resolution of 0.04 mm/pixel. The segments analyzed are 5–6 mm long (200–300 frames per pullback) and cover different plaques (from soft to calcified), morphologies (including branches), and motion artifacts (such as longitudinal motion).

C. Quality Scores

Let us note $\phi^k = \{t_x^k, t_y^k, \theta^k\} = \{p_1^k, p_2^k, p_3^k\}$ the set of motion parameters used to generate the k th frame of a synthetic sequence and $\hat{\phi}^k = \{\hat{t}_x^k, \hat{t}_y^k, \hat{\theta}^k\} = \{\hat{p}_1^k, \hat{p}_2^k, \hat{p}_3^k\}$ the parameters estimated by our algorithm. For each frame k and motion parameter i , we consider the absolute errors (E_i^k) and relative accuracies (ε_i^k) defined [40] as

$$E_i^k = |p_i^k - \hat{p}_i^k| \quad \varepsilon_i^k = \left(1 - \frac{|p_i^k - \hat{p}_i^k|}{p_i^k}\right) * 100$$

These quantities provide, for each sequence and motion parameter, an accuracy function. In order to obtain a single quality

score for each sequence, we consider the maximum and average of accuracy functions over all sequence frames

$$E_i^\infty = \max_k E_i^k, E_i^1 = \frac{1}{N} \sum_{k=1}^N E_i^k, \varepsilon_i^1 = \frac{1}{N} \sum_{k=1}^N \varepsilon_i^k \quad (7)$$

for N the number of frames of each synthetic sequence.

The statistical ranges of the norms (7), given by the mean \pm the variance for all phantoms, indicate the overall accuracy (mean) and stability (variance) of the method. Error ranges are given in pixels for the translation and in degrees (pixel precision in polar coordinates) for the rotation angle.

In the case of CC, normalized cross-correlation [36] is computed between the (whole) image at time k and the reference one and three scores are considered:

- CC_0 : CC average along the original sequence;
- CC_1 : CC average along the processed sequence;
- CAR on CC: defined by (6) as $1 - (A_{CC_1}(\omega_c))/(A_{CC_0}(\omega_c))$.

Image misalignment in IVUS sequences mainly follows from rigid motion [19] and, in our simulated IVUS sequences, only depends on it. It follows that, in our synthetic experiments, images in processed sequences are aligned in the measure that such rigid motion has been properly compensated. Motion is correctly compensated if and only if motion parameters are correctly estimated. Thus, a measure of the increase in image alignment (CDR) and the accuracy in the estimated parameters (ε_3^1) are two different procedures for assessing the same concept (at least in synthetic tests). Statistical analysis comparing means (paired Student t-test with confidence intervals, CI, at 95%) and pdf's (Kolmogorov-Smirnov goodness-of-fit) are used to check whether there is any significant difference between alignment measures and ε_3^1 . We also report Pearsons correlation coefficient and regression coefficients for CDR and ε_3^1 .

VI. EXPERIMENTAL RESULTS

A. Synthetic Data

Table I reports the absolute error ranges (E^1, E^∞) for synthetic motion profiles. Note that errors do not substantially differ between the two synthetic motion profiles considered (periodic and quadratic). As expected, error ranges increase as morphological changes appear (Sequence Model). Regarding the step, there is no difference in E^1 between 1° and 10° . Student (pairwise) t-tests return a p-value equal to 0.99 (CI = $(-0.0098, 0.0091)$) for Static models and equal to 0.98 (CI = $(-0.96, 0.95)$) for Sequence ones.

Fig. 4 shows box plots for $(E_i^1)_{i=1,2,3}$ for *in vivo* profiles and Sequence models. A reference image from each of the sequences is shown at the bottom row. Case1 and Case2 are vessel segments centered at the catheter, Case3 and Case4 are off-center and Case5 is a branch with longitudinal motion. A horizontal line indicates the bound for subpixel accuracy. In general, there is an increase in angular error due to its dependency on the center of mass.

In Table II we summarize the absolute error ranges for *in vivo* motion profiles. Static models achieve subpixel accuracy for average ranges (E^1). As in Table I, errors increase for Sequence

TABLE I
ANGLE ABSOLUTE ERROR RANGES FOR SYNTHETIC PROFILES

	Static Model				Sequence Model			
	1 ^o step		10 ^o step		1 ^o step		10 ^o step	
	E^1	E^∞	E^1	E^∞	E^1	E^∞	E^1	E^∞
Periodic	0.016 ± 0.081	0.032 ± 0.013	0.016 ± 0.008	0.036 ± 0.017	2.215 ± 0.840	4.904 ± 1.446	2.217 ± 0.827	4.934 ± 1.417
Quadratic	0.024 ± 0.017	0.051 ± 0.023	0.025 ± 0.013	0.053 ± 0.016	2.349 ± 1.245	5.164 ± 1.817	2.366 ± 1.316	5.228 ± 1.813

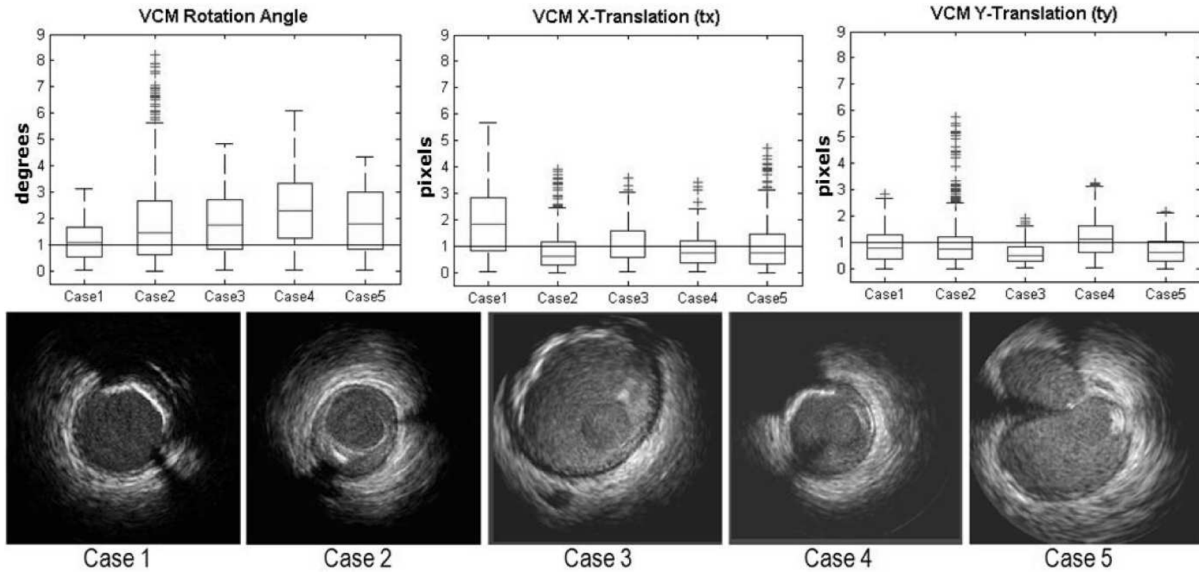


Fig. 4. Box plots for the sequence-based phantoms (first row) and a representative image of the sequence for each phantom (second row).

TABLE II
ABSOLUTE ERROR RANGES FOR *IN VIVO* PROFILES

	Static Model		Sequence Model	
	E^∞	E^1	E^∞	E^1
t_x	1.50 ± 1.23	0.49 ± 0.42	3.48 ± 0.90	1.09 ± 0.58
t_y	1.53 ± 0.88	0.48 ± 0.25	2.94 ± 1.24	0.79 ± 0.16
θ	1.13 ± 0.40	0.34 ± 0.17	4.98 ± 1.50	1.72 ± 0.72

models, although average (E^1) ranges are below 1.67 pixels for translations (t_x) and 2.44° for rotations (θ).

Table III reports the statistics summary for the validation of CDR (using the upper 66% CAR percentile) as accuracy measure. We report ranges for ε_3^1 and CDR, as well as, the (pairwise) t-test p-value and the confidence interval (CI). The right-most three columns are devoted to comparison to normalized cross-correlation measures: CC_0 , CC_1 and CAR on CC. There is no significant difference in means between CDR and ε_3^1 with at most a $\pm 9\%$ of discrepancy. According to a Kolmogorov–Smirnov test for comparison of random variables, there is no evidence of difference in their distributions (with a p-value of 0.3334 and 0.9545 for Static and Sequence phantoms, respectively). Regarding CC, in the absence of morphological changes (Static Model), CC_1 and ε_3^1 ranges are similar. On Sequence phantoms, there is no significant difference between CC_0 and CC_1 , which suggests using the CAR score. However, the global nature of CC, makes CAR on CC underestimate the amount of motion suppressed.

Fig. 5 shows the regression line for the point cloud given by plotting ε_3^1 (X variable) against CDR (Y variable). The regression coefficients for the model $Y = bX + a$ are $b = 0.9315$

and $a = 0.0206$. Pearson’s correlation coefficient (ρ) indicates a significant linear dependency ($\rho = 0.6611$). Finally, the F-statistics for testing $b = 0$ clearly show (with F -pval = $1.1372e^{-5}$) that both scores are correlated.

B. In Vivo Data

Fig. 6 shows four cases with decreasing CDR values (from left to right): 89%, 83%, 75%, and 63%. The first row shows a frame of the original sequences. The corresponding longitudinal cuts at the white lines are shown on the second row and the same cut after sequence alignment on the last one. The sequence in the first column [Fig. 6(a)] presents a structure misalignment due to rotation. The calcium shadow appears and disappears in the original longitudinal cut, whereas it shows a uniform appearance after alignment. In the second column [Fig. 6(b)] translation introduces a saw-shape in the original longitudinal cut (especially at the end of the segment). After compensation, only a faint undulation due to radial dilation remains. The longitudinal cut in Fig. 6(c) shows a straight profile (both before and after alignment) in spite of a lower CDR. This phenomenon, which appears in the absence of motion, is inherent to any relative measure like CDR [40]. Finally, in Fig. 6(d) we show the worst performer, both, in terms of longitudinal cut appearance and CDR value. Since a proper alignment is only achieved at the second half of the segment, we have 63% of motion reduction. Regarding objective measurement of IVUS alignment, we have that the statistical range for CDR gives an overall motion reduction of $82.05\% \pm 6.61\%$.

TABLE III
ALIGNMENT MEASURES VERSUS ANGLE RELATIVE ERROR

	ε_3^1	CDR	p-val	CI	CC_0	CC_1	CAR on CC
Static	95.09 ± 4.63	93.56 ± 4.86	0.3334	(-1.67, 4.73)	89.27 ± 9.46	93.57 ± 8.43	70.95 ± 21.53
Sequence	76.83 ± 13.00	76.59 ± 8.39	0.9545	(-8.60, 9.08)	88.24 ± 6.24	89.58 ± 5.72	28.36 ± 45.63

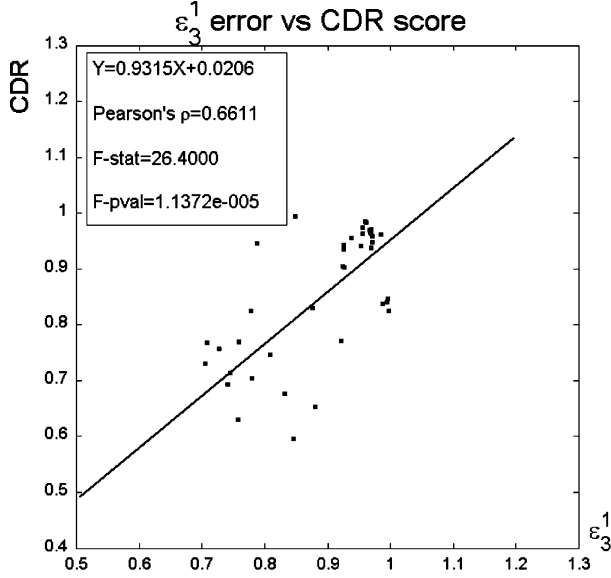


Fig. 5. Linear correlation between CDR and angle relative accuracy (ε_3^1).

C. First Approach to Longitudinal Motion

The first step for modelling longitudinal motion in IVUS sequences is retrieving cardiac phase information. In this section we illustrate our methodology's potential by presenting a first approach to image-based ECG sampling. According to [41], minimum and maximum lumen areas are around the beginning of the QRS complex (end systole) and the T-wave (end diastole) peak in the ECG signal. Luminal area evolution is synchronized to other vessel cardiac phenomena, such as rigid motion or tissue motion. In particular, we have that the extreme values of the local mean evolution LM contain information about cardiac phase. In order to extract it we apply a Butterworth bandpass filter to LM Fourier development [31]

$$H(\omega) = \frac{1}{\sqrt{1 + \left(\frac{\omega - \omega_c}{0.5\Delta\omega}\right)^{2n}}}$$

for ω_c the cardiac frequency defined as in Section III, $n = 4$ and $\Delta\omega = 0.6\omega_c$ as set in [31].

The inverse Fourier transform of the filtered LM signal (HLM) provides, for each image pixel, information about end systole and diastole. In order to retrieve the global phase information, we combine the filtered LM signals. Following the considerations given in Section V-C, we only consider those LM reflecting cardiac motion and define the cardiac phase pattern, CPh, as the average

$$\text{CPh} := \mu(\{\text{HLM} \mid A_{\widehat{\text{LM}}}(\omega_c) > \text{prct}\})$$

for prct the 80% percentile of all LM cardiac amplitudes. The peaks of CPh give a sampling at end diastole, while valleys correspond to end systole [31], [41].

In Fig. 7 we illustrate the performance of our approximation to image-based ECG gating. The top row shows the ECG sampling on a short longitudinal cut at a side branch. The left image corresponds to the original cut with the side branch on the upper half. The image on the right shows the sampling given by CPh peaks in dashed lines. We note that peak match the extreme points of the longitudinal profile. On the bottom row, we show two large (over 5 cm) longitudinal cuts (left images) sampled at end diastole rate (right images).

VII. DISCUSSION AND CONCLUSION

This paper approaches compensation and assessment of artery rigid dynamics in IVUS sequences. We address cardiac rigid motion and define an objective score (CDR) measuring motion reduction in experimental data. We present experiments on synthetic sequences and *in vivo* pullbacks. Synthetic experiments serve to assess the accuracy of the motion estimation and validate CDR as quality measure. For *in vivo* pullbacks we present a first approximation to longitudinal motion.

By combining vessel appearance and shape, we provide explicit formulae for motion parameters. This sets no limits to the capture range of motion parameters and we have equal performance (Table I) for frame-to-frame steps of 1 and 10. Translation is given (independently for each frame) in absolute terms, whereas rotation is computed by accumulating frame-to-frame transformations. In large segments, the latter might introduce accumulation errors. Alignment of large segments is a difficult task, due to morphological variations, which also might drop the accuracy of registration algorithms. Therefore, we consider that this does not represent a major limitation of our approach compared to registration strategies. Experiments on sequence-based synthetic models (Table II) show that the main source of error arises from morphological changes along the vessel, with average errors of 1.09 pixels * 0.04 mm/pixel = 0.044 mm for translations and 1.72° for rotations. Our errors favorably compare to the numbers reported in [12], which achieve mean errors of 0.064 mm and 7.8°, provided that the catheter rotation does not exceed 3.5°.

Our quality measure bases on the conservation of the image local density of mass (given by the local mean) and only considers image pixels with noticeable motion. Results on Sequence models (Table III) show that CDR correlates to the angular relative accuracy. Results on real pullbacks show that, in general, CDR also correlates to the uniform and continuous appearance of longitudinal cuts [see Fig. 6(a), (b), and (d)]. This fact validates CDR as an objective measure of image alignment. Comparison to global similarity scores, such as cross-correlation (Table III), indicates that global approaches are prone to underestimate motion reduction.

Experimental results detect two sources for under performance of the proposed methodology: sudden morphological changes and nonperiodic random motion patterns. In the first

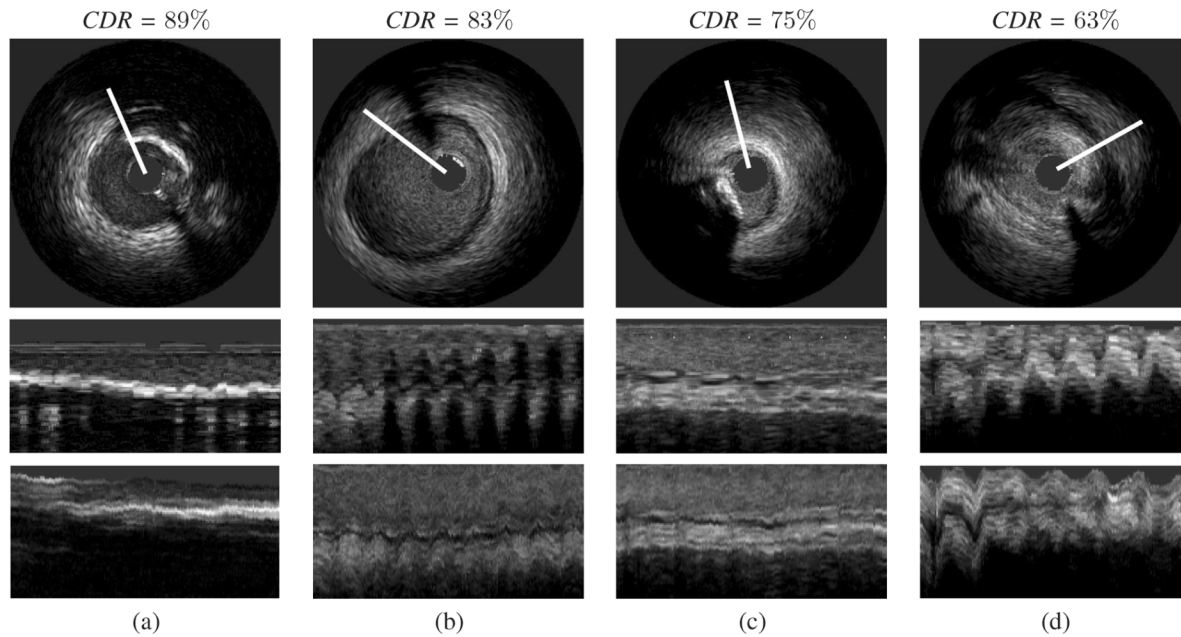


Fig. 6. Longitudinal cuts for sequences of four different patients (columns), from the best corrected sequence (a) to the worst corrected one (d). Original frames are shown on the first row, original longitudinal cuts on the second row, and corrected ones on the third row.

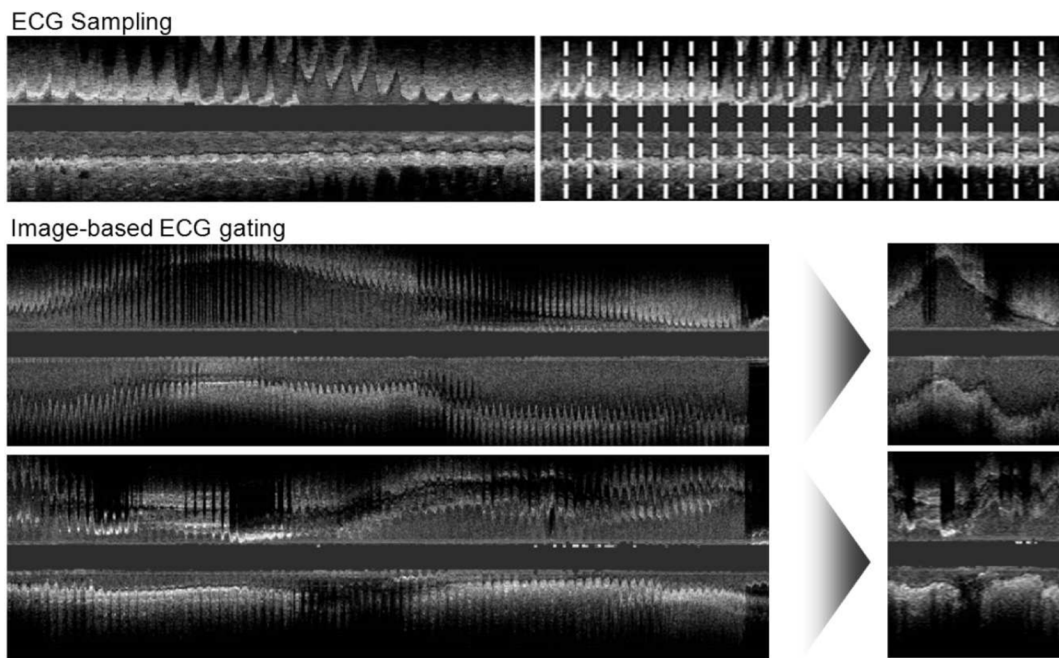


Fig. 7. Image-based ECG sampling of a short segment (top) and gating images of long cuts (bottom).

case, which is a common limitation in most registration and tracking algorithms, changes in appearance mislead image alignment as the objects to be tracked have significantly changed. The second source of error is inherent to the definition of rigid (periodic) movement, which is the only motion considered. These extreme cases, which CDR might drop to 63%, only represent a 6% of the data analyzed.

Although we do not explicitly address it, the developed methods allow exploring longitudinal motion. Longitudinal motion affects 3-D IVUS exploring in two main ways.

- 1) 3-D vessel measurements and visualization. Reliable 3-D measurements along the vessel must either account (i.e., correct) for catheter swinging or simulate image-based

ECG-gating [7], [42]. In Section VI-C we illustrate the potential of the methods presented by giving a first approximation to image-based ECG gating (Fig. 7).

- 2) Biomechanics analysis. Longitudinal motion might disturb computation of tissue properties only in the case of a segment with a transition between two different kind of plaque. Since, if noticeable, longitudinal motion induces a periodic variability in tissue composition, CDR allows its detection and, thus, selection of those segments best suited for assessing biomechanics.

By the former considerations we conclude that the methods presented are suitable for exploring tissue mechanical properties from *in vivo* clinical cases.

REFERENCES

- [1] J. Wentzel, R. Krams, J. H. Schuurbiers, J. Oomen, J. Kloet, W. van der Giessen, P. Serruys, and C. Slager, "Relationship between neointimal thickness and shear stress after wallstent implantation in human coronary arteries," *Circulation*, vol. 103, no. 13, pp. 1740–5, 2001.
- [2] J. Garcia, A. Crespo, J. Goicolea, M. Sanmartin, and C. Garcia, "Study of the evolution of the shear stress on the restenosis after coronary angioplasty," *J. Biomechan.*, vol. 39, no. 5, pp. 799–805, 2006.
- [3] I. Kakadiaris, S. O'Malley, M. Vavuranakis, S. Carlier, R. Metcalfe, C. Hartley, E. Falk, and M. Naghavi, "Life-sciences signal-processing approaches to risk assessment in coronary artery disease," *IEEE Signal Process. Mag.*, vol. 23, no. 6, pp. 59–62, Nov. 2006.
- [4] E. Cespedes, C. Korte, and A. van der Steen, "Intraluminal ultrasonic palpation: Assessment of local and cross-sectional tissue stiffness," *Ultrasound Med. Biol.*, vol. 26, no. 3, pp. 385–396, Mar. 2000.
- [5] P. Delachartre, C. Cachard, G. Finet, F. Gerfault, and D. Vray, "Modeling geometric artefacts in intravascular ultrasound imaging," *Ultrasound Med. Biol.*, vol. 25, no. 4, pp. 567–575, May 1999.
- [6] N. Bruining, C. von Birgelen, P. J. de Feyter, J. Ligthart, W. Li, P. Serruys, and J. R. Roelandt, "ECG-gated versus nongated three-dimensional intracoronary ultrasound analysis: Implications for volumetric measurements," *Catheter Cardiovasc. Diagn.*, vol. 43, no. 3, pp. 254–260, Mar. 1998.
- [7] C. von Birgelen, G. Mintz, A. Nicosia, D. P. Foley, W. J. van der Giessen, N. Bruining, S. Airiian, J. T. C. Roelandt, P. de Feyter, and P. Serruys, "Electrocardiogram-gated intravascular ultrasound image acquisition after coronary stent deployment facilitates on-line three-dimensional reconstruction and automated lumen quantification," *J. Amer. College Cardiol.*, vol. 30, no. 2, pp. 436–443, Aug. 1997.
- [8] A. Wahle, S. C. Mitchell, S. D. Ramaswamy, K. Chandran, and M. Sonka, "Four-dimensional coronary morphology and computational hemodynamics," in *SPIE Med. Imag. 2001: Image Process. Conf.*, Feb. 2001, vol. 4322, pp. 743–754.
- [9] Y. Shi, F. de Ana, S. Chetcuti, and M. O'Donell, "Motion artifact reduction for IVUS-based thermal strain imaging," *IEEE Trans. Ultrason. Ferroelectr. Freq. Control*, vol. 52, no. 8, pp. 1312–1319, Aug. 2005.
- [10] K. Y. E. Leung, R. Baldewsing, F. Mastik, J. Schaar, and D. Gisol, "Motion compensation for intravascular ultrasound palpography," *IEEE Trans. Ultrason. Ferroelectr. Freq. Control*, vol. 53, no. 7, pp. 1269–1280, Jul. 2006.
- [11] A. Arbab-Zadeh, A. DeMaria, W. Penny, R. Russo, B. Kimura, and V. Bhargava, "Axial movement of the intravascular ultrasound probe during the cardiac cycle: Implications for three-dimensional reconstruction and measurements of coronary dimensions," *Amer. Heart J.*, vol. 138, no. 5, pp. 865–872, 1999.
- [12] M. Danilouchkine, F. Mastik, and A. van der Steen, "Accuracy in prediction of catheter rotation in IVUS with feature-based optical flow: A phantom study," *IEEE Trans. Inf. Tech. Biomed.*, vol. 12, no. 3, pp. 356–365, May 2008.
- [13] Y. Saijo, A. Tanaka, N. Owada, Y. Akino, and S. Nitta, "Tissue velocity imaging of coronary artery by rotating-type intravascular ultrasound," *Ultrasonics*, vol. 42, pp. 753–757, Apr. 2004.
- [14] B. Zitova and J. Flusser, "Image registration methods: A survey," *Image Vis. Comput.*, vol. 21, no. 11, pp. 977–1000, Oct. 2003.
- [15] A. Hernandez, P. Radeva, A. Tovar, and D. Gil, "Vessel structures alignment by spectral analysis of IVUS," in *Comput. Vis. Intravascular Imag.*, Oct. 2006, pp. 30–37.
- [16] J. Mazumdar, *Biofluids Mechanics*. Singapore: World Scientific, 1992.
- [17] S. Nadkarni, H. Austin, G. Mills, D. Boughner, and A. Fenster, "A pulsating coronary vessel phantom for two- and three-dimensional intravascular ultrasound studies," *Ultrasound Med. Biol.*, vol. 29, no. 4, pp. 621–628, Apr. 2003.
- [18] G. Holzapfel, T. Gasser, and M. Stadler, "A structural model for the viscoelastic behavior of arterial walls: Continuum formulation and finite element analysis," *Eur. J. Mech. A. Solids*, vol. 23, pp. 1–162, 2002.
- [19] E. Waks, J. L. Prince, and A. Douglas, "Cardiac motion simulator for tagged MRI," in *Proc. Math. Methods Biomed. Image Anal.*, Jun. 1996, pp. 182–191.
- [20] H. Goldstein, C. Poole, and J. Safko, *Classical Mechanics*, 3rd ed. Reading, MA: Addison Wesley, 2002.
- [21] I. Fontaine, M. Bertrand, and G. Cloutier, "A system-based approach to modeling the ultrasound signal backscattered by red blood cells," *Biophys. J.*, vol. 77, no. 5, pp. 2387–2399, Nov. 1999.
- [22] M. Resales, P. Radeva, J. Mauri, and O. Pujol, "Simulation model of intravascular ultrasound images," in *Proc. MICCAI*, Sep. 2004, vol. 3217, pp. 200–7.
- [23] G. Mintz and S. Nissen, "Clinical expert consensus document on standards for acquisition, measurement and reporting of intravascular ultrasound studies (IVUS)," *JACC*, vol. 37, no. 5, pp. 1478–92, 2001.
- [24] K. Caballero, J. Barajas, O. Pujol, N. Salvatella, and P. Radeva, "In-vivo IVUS tissue classification: A comparison between RF signal analysis and reconstructed images," in *Progress in Pattern Recognition, Image Analysis and Applications*. New York: Springer, Nov. 2006, vol. 4225, Lecture Notes in Computer Science, pp. 137–146.
- [25] D. Gil, A. Hernandez, O. Rodriguez, J. Mauri, and P. Radeva, "Statistical strategy for anisotropic adventitia modeling in IVUS," *IEEE Trans. Med. Imag.*, vol. 25, no. 6, pp. 768–778, Jun. 2006.
- [26] M. D. Resales, "A physics-based image modelling of IVUS as a geometric and kinematics system," Ph.D. dissertation, Univ. Autonoma de Barcelona, Barcelona, Spain, 2005.
- [27] A. Oppenheim and A. Willsky, *Signals and Systems*, 2nd ed. Englewood Cliffs, NJ: Prentice-Hall, 1997.
- [28] C. Kuglin and D. Hines, "The phase correlation image alignment method," in *Proc. IEEE Conf. Cybern. Soc.*, Sep. 1975, pp. 163–165.
- [29] S. Alliney, "Spatial registration of multispectral and multitemporal digital imagery using fast-fourier transform techniques," *IEEE Pattern Anal. Mach. Intell.*, vol. 15, no. 5, pp. 499–504, 1993.
- [30] D. Rotger, P. Radeva, and O. Rodriguez, "Vessel tortuosity extraction from IVUS images," in *Comp. Cardiol.*, Sep. 2006, pp. 689–692.
- [31] H. Zhu, K. D. Oakeson, and M. H. Friedman, "Retrieval of cardiac phase from IVUS sequences," in *Proc. SPIE Med. Imag.: Ultrason. Imag. Signal Process.*, 2003, vol. 5035, pp. 135–146.
- [32] D. Gil, O. Rodriguez-Leor, P. Radeva, and J. Mauri, "Myocardial per-fusion characterization from contrast angiography spectral distribution," *IEEE Trans. Med. Imag.*, vol. 27, no. 5, pp. 641–649, May 2008.
- [33] S. Mallat, *A Wavelet Tour of Signal Processing*. San Diego, CA: Academic, 1998.
- [34] A. Klug and D. J. DeRosier, "Optical filtering of electron micrographs: Reconstruction of one-sided images," *Nature*, vol. 212, no. 5057, pp. 29–32, Oct. 1966.
- [35] P. Viola and W. Wells, "Alignment by maximization of mutual information," *Int. J. Comput. Vis.*, vol. 24, no. 2, pp. 137–154, 1997.
- [36] W. Pratt, *Digital Image Processing*, 2nd ed. New York: Wiley, 1991.
- [37] J. P. W. Pluim, J. B. A. Maintz, and M. A. Viergever, "Mutual-information-based registration of medical images: A survey," *IEEE Trans. Med. Imag.*, vol. 22, no. 8, pp. 986–1004, Aug. 2003.
- [38] S. Whitaker, *Introduction to Fluid Mechanics*. Melbourne, FL: Krieger, 1992.
- [39] P. Rousseeuw and A. Leroy, *Robust Regression and Outlier Detection*. New York: Wiley, 1987.
- [40] R. Burden and J. Faires, *Numerical Analysis*. Florence, KY: Brooks-Cole, 2004.
- [41] J. Shaw, B. Kingwell, A. Walton, J. Cameron, P. Pillay, C. Gatzka, and A. Dart, "Determinants of coronary artery compliance in subjects with and without angiographic coronary artery disease," *J. Amer. College Cardiol.*, vol. 39, no. 10, pp. 1637–1643, 2002.
- [42] S. Winter, R. Hamers, M. Degertekin, K. Tanabe, P. Lemos, P. Serruys, J. R. Roelandt, and N. Bruining, "Retrospective image-based gating of intracoronary ultrasound images for improved quantitative analysis: The intelligent method," *Catheter Cardiovasc. Interv.*, vol. 61, no. 1, pp. 84–94, Jan. 2004.